

Photodissociation dynamics of the N₃ radical

R. E. Continetti,^{a)} D. R. Cyr,^{b)} D. L. Osborn,^{c)} D. J. Leahy, and D. M. Neumark^{d)}
*Department of Chemistry, University of California, Berkeley, California 94720 and Chemical Sciences
Division, Lawrence Berkeley Laboratory, Berkeley, California 94720*

(Received 22 December 1992; accepted 27 April 1993)

The dissociation dynamics of the $\tilde{B}^2\Sigma_u^+$ state of N₃ were investigated using fast radical beam photodissociation coupled with a new coincidence wedge-and-strip-anode particle detector. With this detector, detailed photofragment kinetic energy and angular distributions can be measured as a function of excitation energy. Calibration of the detector by studies of the predissociation of the O₂ $B^3\Sigma_u^-$ state is discussed. Methods of extracting the center-of-mass kinetic energy and angular distributions are presented. The photodissociation results for N₃ show that from the vibrationless level of the $\tilde{B}^2\Sigma_u^+$ state in N₃, both spin-allowed [N₃ → N(²D) + N₂(¹Σ_g⁺)] and spin-forbidden [N₃ → N(⁴S) + N₂(¹Σ_g⁺)] dissociation processes occur. Bend excitation in the $\tilde{B}^2\Sigma_u^+$ state, however, enhances the spin-allowed dissociation process considerably. The kinetic energy distributions reveal partially resolved vibrational structure in the N₂ fragment, and indicate substantial rotational excitation of the N₂. This implies that bent geometries play a major role in the dissociation of the N₃ \tilde{B} state. Possible mechanisms for the spin-forbidden and spin-allowed dissociation channels are discussed.

I. INTRODUCTION

The study of molecular photodissociation dynamics, first proposed 30 years ago,¹ has proved to be an extremely powerful tool in gaining a fundamental understanding of the interactions among excited electronic states in diatomic and polyatomic molecules. An impressive array of experimental techniques has been developed which allow detailed characterization of the photofragments resulting from photodissociation.² These include photofragment translational spectroscopy,³⁻⁶ in which one measures the translational energy and/or the angular distribution of the photodissociation products, state-resolved photofragment detection,⁷ in which the internal energy of one or more of the photofragments is spectroscopically determined, and techniques such as Doppler spectroscopy^{8,9} and photofragment imaging¹⁰ which yield the kinetic energy and angular distribution associated with a selected internal photofragment state.

The vast majority of photodissociation experiments performed thus far has involved stable, closed-shell molecules. In contrast, detailed measurements of photofragment properties have been made for only a handful of reactive free radicals.¹¹⁻¹⁴ This is due, in large part, to the difficulties inherent in the production of well-characterized free radicals. We have recently demonstrated a new approach to free radical photodissociation in which photodetachment of a fast negative ion beam is used to produce state-selected neutral radicals for subsequent photodissociation studies.^{15,16} The fast-beam approach builds on studies of dissociative states of small molecules produced via charge ex-

change, pioneered in Los' group¹⁷⁻¹⁹ and used by Helm and Cosby as well.²⁰ In our experiment, we produce state-selected polyatomic free radicals by laser photodetachment of a mass-selected fast (8 keV) negative ion beam. The free radicals are then photodissociated by a second laser, and the neutral photofragments detected with high efficiency. Since most free radicals have a positive electron affinity, and therefore a corresponding stable anion, this provides a general route to the study of the photodissociation dynamics of these species.

Thus far, we have used this method to measure the photodissociation cross section and photofragment kinetic energy release for N₃ (Ref. 15) and NCO.¹⁶ In this paper, we describe new results on N₃ obtained with a more sophisticated photofragment coincidence detection scheme, conceptually similar to that reported by Los,¹⁷ which enhances our ability to perform photofragment translational spectroscopy experiments on the products of free radical photodissociation. In particular, we obtain considerably more detailed photofragment kinetic energy and angular distributions than were attainable in our original study on N₃.

The N₃ free radical has received considerable attention in recent years due to its importance in chemical-laser pumping reactions. Research in this area is ongoing; several kinetics measurements of the reaction of N₃ with halogen atoms have recently been reported.^{21,22} Such studies are increasingly taking advantage of the numerous spectroscopic techniques²³⁻²⁶ applied to this radical since the electronic absorption spectrum [the $\tilde{B}^2\Sigma_u^+ \leftarrow \tilde{X}^2\Pi_g$ transition near 270 nm (Ref. 27)] was first recorded by Thrush²⁸ in 1956 and assigned by Douglas and Jones²⁹ in 1965. There has also been substantial effort devoted to an understanding of the energetics of N₃ (see Fig. 1). The most recent previous experiments to bear directly on the question of the stability of N₃ were the proton affinity studies of N₃⁻ (Ref. 30) and the electron affinity studies of N₃ (Refs. 31, 32) by

^{a)}Permanent address: Department of Chemistry, University of California, San Diego, La Jolla, California 92093-0314.

^{b)}NSERC (Canada) 1967 Predoctoral Fellow.

^{c)}NDSEG Predoctoral Fellow.

^{d)}NSF Presidential Young Investigator and Camille and Henry Dreyfus Teacher-Scholar.

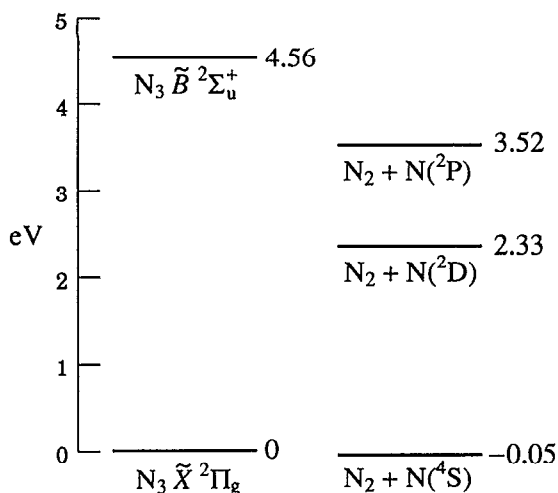


FIG. 1. Energetics (in eV) of the N₃ system. The present experiments find that N₃ is unstable with respect to N(⁴S)+N₂, with $D_0 = -0.05 \pm 0.10$ eV.

Brauman and co-workers. These experiments were interpreted to show that N₃ is roughly thermoneutral relative to N(⁴S)+N₂, the lowest energy (but spin-forbidden) channel, with $D_0(\text{N}_2-\text{N}) = -0.01 \pm 0.22$ eV.³³ The energetics of N₃ have also been investigated in quantum chemistry calculations. The most recent calculation by Martin *et al.*³⁴ gives $\Delta H_{f,0}^0(\text{N}_3) = 109.2 \pm 2$ kcal/mol (4.73 ± 0.09 eV), from which $D_0 = +0.14 \pm 0.09$ eV, in reasonable agreement with the experimental determination of Brauman and co-workers. Our results provide a direct, independent experimental determination of the N₃ bond dissociation energy.

Quantum chemistry calculations on the electronic and vibronic structure of N₃ are difficult since it is an open-shell system. There have been several recent studies, however, including structure and vibrational frequencies of both N₃ and N₃⁻ by Kaldor,³⁵ a study by Chambaud and Rosmus³⁶ of the rovibronic structure of the ground state of N₃, and the study of the dissociation energy of N₃ by Martin mentioned above. Thus far, the only theoretical work on the excited electronic states of N₃ is the work of Petrongolo.³⁷ This work, which was restricted to linear geometries, indicates that in addition to the $\tilde{B}^2\Sigma_u^+$ state, a bound ⁴Π state should lie nearby as well, which may perturb the $^2\Sigma_u^+$ levels and give rise to the as-yet unassigned bands seen in absorption near 270 nm.²⁹

The $\tilde{B} \leftarrow \tilde{X}$ transition in N₃ is quite interesting from the viewpoint of photodissociation. Although the assigned $\tilde{B} \leftarrow \tilde{X}$ transitions are fully rotationally resolved,²⁹ the $\tilde{B}^2\Sigma_u^+$ state lies at least 4.5 eV above the N(⁴S)+N₂ channel, and also well above the spin-allowed N(²D)+N₂ and N(²P)+N₂ channels. However, there had been no studies of the gas-phase photodissociation dynamics until our recent work applying the fast beam photodissociation technique to the $\tilde{B}^2\Sigma_u^+$ state.¹⁵ Our previous work showed that *all* levels of the \tilde{B} state predissociate readily on a time scale much shorter than 5 μs. In addition, our photofragment time-of-flight measurements of the kinetic energy released

in the dissociation indicated that the primary dissociation products were N(²D)+N₂, consistent with previous matrix-isolation studies which revealed N(²D)→N(⁴S) phosphorescence after ultraviolet (UV) irradiation.³⁸ To better determine the N₃ photodissociation branching ratios, and, in particular, to further investigate the possibility of spin-forbidden dissociation processes, we have re-examined this system with our new photofragment coincidence detection scheme.

The studies reported here were also motivated by results on electronic branching in the predissociation of similar molecules. For example, we have examined predissociation from the $\tilde{B}^2\Pi$ state of NCO, which is isoelectronic with N₃, and observed that both spin-allowed and spin-forbidden dissociation processes play a major role in this predissociation.¹⁶ In contrast to the $\tilde{B}^2\Sigma_u^+$ state in N₃, the lowest vibrational levels of the NCO $\tilde{B}^2\Pi$ state can dissociate only to the spin-forbidden N(⁴S)+CO channel. However, once the spin-allowed N(²D) channel becomes energetically accessible it rapidly becomes the dominant dissociation pathway. In contrast, a recent study by Guyon and co-workers³⁹ of the predissociating $\tilde{A}^2\Sigma^+$ state of N₂O⁺ (also isoelectronic with N₃) suggests that the branching ratio between the spin-forbidden N(⁴S)+NO⁺ and spin-allowed N(²D)+NO⁺ channels varies markedly with internal excitation of the N₂O⁺, even at energies where both channels are accessible. For example, the branching ratio is quite different for the nearly isoenergetic (101) and (300) levels of the $\tilde{A}^2\Sigma^+$ state. Hepburn and co-workers⁴⁰ have also recently found that the branching ratio between spin-forbidden and spin-allowed dissociation channels in CS₂ depends strongly on the vibrational level of the dissociating CS₂ state. Finally, Davis and Lee¹⁴ have seen mode-selective effects in the predissociation of the ClO₂ \tilde{A} state. In their study, concerted elimination of O₂ was promoted by both bending excitation and combinations of symmetric and antisymmetric stretches. These results, and similar phenomena observed in direct photodissociation processes,⁴¹⁻⁴³ present a considerable theoretical challenge as they must result from the interaction of multiple excited electronic states.

In the following sections, we describe the apparatus and the newly installed coincidence detector used in our photodissociation dynamics experiments. We then discuss calibration experiments using the predissociation of the O₂ $B^3\Sigma_u^-$ state excited in the Schumann-Runge band, followed by the new N₃ photodissociation results. Two methods of analyzing the raw data, a Monte Carlo forward convolution and a direct numerical analysis of the detector acceptance, are then described and applied to extract the center-of-mass kinetic energy and angular distributions from the raw data. Our results have confirmed that N(²D) is in fact the primary photoproduct, but we have observed significant N(⁴S) products originating from the predissociation of the lowest vibrational level of the \tilde{B} state. This measurement reveals that in the N₃ system, both spin-allowed and spin-forbidden dissociation can occur from the \tilde{B} state, with bend excitation strongly favoring the spin-allowed product channel. We also obtain detailed N₂ inter-

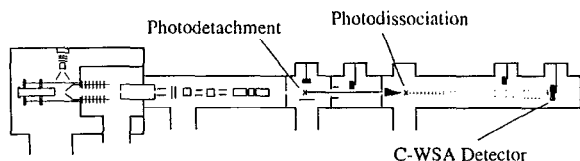
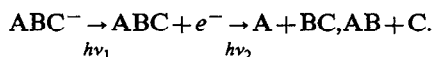


FIG. 2. The fast radical beam photofragment spectrometer. See general discussion in text and Ref. 15. The photodetachment and photodissociation interaction regions are shown, with a representative pair of fragments recoiling out of the beam axis shown by the dotted lines. The coincidence wedge-and-strip anode (C-WSA) detector is discussed in the text.

nal energy distributions corresponding to each N atom electronic state; these yield considerable insight into the photodissociation dynamics of the N_3 radical.

II. EXPERIMENT

In order to study the photodissociation of a generic free radical, ABC, we first generate a fast (8 keV) beam of the mass-selected precursor anion ABC^- , then photodetach the anion with a pulsed laser, forming ABC with a known internal energy distribution. The radical is photodissociated with a second pulsed laser, and the photofragments are detected,



The kinematics of fast beam dissociation are such that a large fraction of the photofragments impinge on the detector. Thus, by monitoring the total photofragment yield as a function of $h\nu_2$, we can map out the photodissociation cross section for the ABC radical. In the past, we also obtained approximate photofragment energy distributions by measuring the arrival time distribution of the fragments at the detector. The newly installed coincidence detector provides a considerably richer picture of the photodissociation dynamics than our previous measurements. This detector yields the position of the two photofragments and the time delay between their arrival, enabling us to determine the center-of-mass kinetic energy, scattering angle, and fragment mass ratio directly for each photodissociation event. The detector is conceptually similar to the design of DeBruijn and Los,¹⁷ but the position and time sensing is accomplished using a coincidence wedge-and-strip anode (C-WSA) assembly rather than by capacitive charge division.

Most features of the fast radical beam photofragment spectrometer used in this study have been previously described in detail.^{15,16} Below, we give a short overview of the apparatus followed by a more detailed discussion of the new detector. A schematic of the apparatus is shown in Fig. 2.

A. Fast radical beam photofragment spectrometer

In these experiments, we use O_2^- and N_3^- as precursors to the neutrals under study. The pulsed beam source used to produce these anions is similar to that developed by Lineberger and co-workers,⁴⁴ and has been previously used

in our laboratory.⁴⁵ A 1 keV electron beam crosses a pulsed, free-jet expansion of either neat O_2 or benzyl azide seeded in Ne. Low energy secondary electrons produce N_3^- by dissociative attachment to benzyl azide, as first shown by Illenberger and co-workers.³² The mechanism for O_2^- formation is not as clear, but probably involves dissociative attachment to O_2 clusters, or some other many-body process. The nascent negative ions are subsequently cooled in the free-jet expansion, and then pass through a 3 mm skimmer into a differentially pumped region where they are accelerated to energies up to 8 keV. An einzel lens in the acceleration stack is used to mildly focus the ion beam. After acceleration, the anions pass into a potential switch,^{46,47} where they are conveniently rereferenced to ground potential, while retaining their translational energy.

After exiting the potential switch, a set of beam modulation plates is used to select a short pulse of ions for time-of-flight mass spectroscopy, as first described by Bakker.⁴⁸ The ions then enter an axial pulsed field which is used to compress the ion pulse to allow optimum spatial and temporal overlap with the pulsed lasers. This field induces an energy spread of ≈ 70 eV in the O_2^- ion beam, but this spread of $< 1\%$ in the primary beam energy has no significant effect on the experiments reported here. The ions then pass through sets of horizontal and vertical deflectors which assist in guiding the ion beam through the 1 mm apertures that define the beam axis, and a second einzel lens used for mild focusing.

At a distance of 0.86 m from the beam modulation plates, the ions pass through a 1 mm aperture into the detachment region. At the center of this region, an excimer-pumped dye laser pulse intercepts the ions at the mass of interest, resulting in the production of neutrals by photodetachment. We detach O_2^- at 540 nm, using Coumarin 540 A (Exciton) laser dye, and N_3^- is detached at 343 nm, using PTP (Exciton), with fluences of ≈ 1 J/cm². In the case of O_2^- , detachment at 540 nm produces O_2 in both the ground $X^3\Sigma_g^-$ and first excited $a^1\Delta$ states; the vibrational distribution for the $X^3\Sigma_g^-$ state peaks at $v=2$, with significant population extending out to $v=5$.⁴⁹ As is evident from the N_3^- photoelectron spectrum,¹⁵ photodetachment of N_3^- well above threshold does not excite any vibrational modes, although any vibrational excitation in the anion will be transferred to the radical upon photodetachment. The detached electrons are extracted by a 5 V pulse and detected by a 25 mm diam chevron microchannel-plate detector; this allows us to monitor the neutral beam intensity. For O_2^- and N_3^- , up to 80% detachment can be achieved. The beam, now composed of a mixture of neutrals and anions, passes through a 3 mm aperture, after which ions are deflected out of the beam by a 2 kV dc field, into a second microchannel-plate detector which is used to monitor the ion beam.

The mass-selected neutral beam then passes through a final 1 mm aperture into the dissociation and detection region. The highly-collimated beam (angular full-width-at-half-maximum $< 0.07^\circ$) is intercepted by the photodissociation laser, a second excimer-pumped pulsed dye laser; the

photodissociation interaction volume is $\approx 1 \text{ mm}^3$. Since the O₂ $X^3\Sigma_g^-$ produced by photodetachment is vibrationally excited, we can excite the $v'=7 \leftarrow v''=4$ transition of the well-known Schumann-Runge bands at $\approx 210.2 \text{ nm}$.⁵⁰ This wavelength is produced by frequency doubling the output of Exalite 416 (Exciton) in a BBO crystal. N₃ is photodissociated near 270 nm using light produced by doubling the output of C540A in BBO. Typical dissociation laser fluences of 0.05 J/cm² are used. In the results reported here, the laser polarization is parallel to the beam axis.

The nascent photofragments recoil out of the beam path and strike the active area of one of two detectors, each of which consists of a stack of microchannel plates. One detector, located 0.68 m from the photodissociation interaction volume, is used for measuring total photofragment flux; this detector can be moved entirely out of the radical beam path. The second detector, which lies 1.00 m from the interaction volume, is time and position sensitive. Both detectors have metal strips across their center lines to prevent the undissociated radicals from reaching the active area. The photofragments have laboratory energies in excess of 2 keV, and those that recoil out of the beam and strike the active area of a detector are detected with high efficiency ($\sim 50\%$). The movable detector, which is described in our previous papers, is lowered into the radical beam for measurements of the photofragmentation cross section as a function of dissociation wavelength. The new time and position sensitive detector is described in the following section.

B. Coincidence wedge-and-strip-anode particle detector

Time- and position-sensitive detectors have previously been used in studies of metastable neutral dissociation and photodissociation processes.¹⁷⁻²⁰ The majority of the studies to date have used one-dimensional (radial) position-sensitive detection, which can only measure photofragment angular distributions in specific experimental geometries. However, two-dimensional position-sensitive detectors have seen application in a variety of electron spectroscopies.⁵¹ The results in this paper were obtained with a detector that combines time- and two-dimensional position-sensing. Schins *et al.*⁵² have recently developed a detector with similar capabilities and applied it to charge-transfer studies of high energy ion beams at surfaces. In our detector, position sensing of the two photofragments is accomplished with a specially designed anode assembly that sits behind the microchannel plates. This assembly consists of two wedge-and-strip anodes⁵³ side-by-side; details are given below. This design was chosen over several other possible methods.⁵⁴ Resistive anodes and charge-coupled-device-based imaging methods have slower time responses, and are thus not ideal for timing purposes.^{51,55} Multianode array techniques⁵⁶ with multiple-event capabilities were also considered, but implementation of such detectors is a very expensive proposition.

The principle of this technique relies on the detection of the two photofragments from a single dissociation event

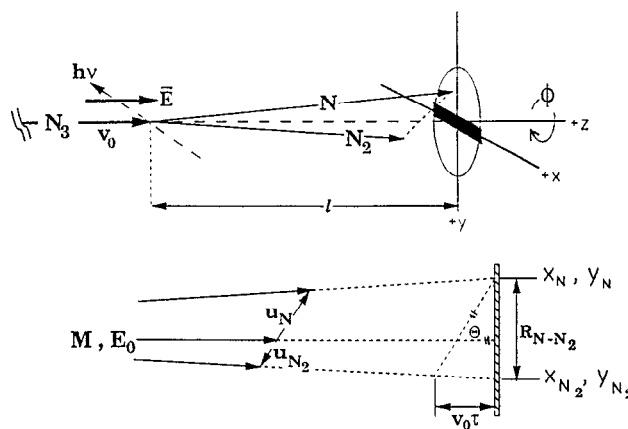


FIG. 3. Kinematics of the coincidence time- and position-sensitive detector experiment in a fast beam. In this figure, N₃ has taken the role of ABC, with N and N₂ taking the role of A and BC in the text discussion. Note the coordinate system and the orientation of the electric field vector **E** used in these experiments. The top diagram in particular is not to scale; the N₃ beam velocity is ≈ 40 times greater than the CM recoil velocities of the N and N₂ fragments.

in coincidence. Although single particle detection can be used in fast beam photodissociation experiments,⁵⁷ the coincidence measurement is required for direct determination of the masses of the photofragments and the center-of-mass dynamical quantities for each dissociation event. The application of a radial coincidence time- and position-sensitive detector to the study of molecular dissociation dynamics, including the kinematic equations that relate position and relative time-of-arrival of the particles to center-of-mass angle and kinetic energy release, was discussed in detail by DeBrujin and Los.¹⁷ With the exception of an inconsistent sign convention, these kinematic equations are used in these studies as well (see Fig. 3). Given the parent mass *M*, flight length, *l*, primary beam velocity *v*₀ or energy *E*₀, the measured separation of the two fragments *R* and the coincidence time τ , the center-of-mass angle θ is given by

$$\theta = \tan^{-1} \left(\frac{R}{v_0 \tau} \right), \quad (1)$$

where τ is defined to be positive when *A* reaches the detector first. The center-of-mass kinetic energy release (henceforth referred to as KER), is given by

$$E_{\text{CM}} = \left(\frac{E_0}{l^2} \right) \left(\frac{m_A m_{\text{BC}}}{M^2} \right) [(v_0 \tau)^2 + R^2] \\ \times \left(1 + 2 \frac{m_{\text{BC}} - m_A}{M} \frac{v_0 \tau}{l} \right). \quad (2)$$

From the quantity *R*_{BC}, the distance that the cofragment BC traveled from the center of radical beam, the masses of the photofragments can be found. For example,

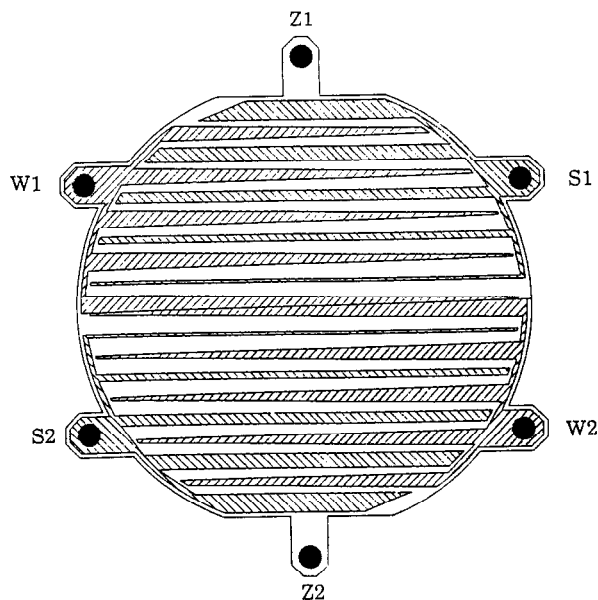


FIG. 4. Schematic layout of the coincidence wedge-and-strip anode. This five period pattern is for illustrative purposes only—the actual anode has 32 periods per half. W1,S1,Z1 and W2,S2,Z2 measure the charges for the upper and lower halves of the detector, respectively. The wedges and strips are hatched in this figure. The solid lines separating the conductors represent insulating gaps.

$$m_A = M \cdot R_{BC} \frac{\left(1 - \frac{v_0 \tau}{l}\right)}{\left[R - \left(\frac{v_0 \tau}{l}\right) R_{BC}\right]} \quad (3)$$

In contrast to the original detector of DeBrujin and Los, which measures the radial displacements of the two fragments from the detector center, our detector yields the particle displacements (x_A, y_A) and (x_{BC}, y_{BC}) in two dimensions. This has two advantages. First, a two-dimensional detector is needed to measure the photofragment angular distributions in experiments where the electric field vector \mathbf{E} of the dissociation laser is perpendicular to the beam axis, since the photofragments are no longer azimuthally symmetric about the ion beam direction. Second, two-dimensional imaging helps discriminate against false coincidences, since

$$\frac{x_{BC}}{x_A} = \frac{y_{BC}}{y_A} \quad (4)$$

must be satisfied due to conservation of momentum if the two photofragments originated from the same photodissociation event.

The principle of the wedge-and-strip-anode⁵³ is to divide the cloud of charge from a microchannel plate detector between separate conductors on the anode in a spatially specific manner. This charge division between the conductors is determined simply by their geometric areas. A schematic layout of the C-WSA used in these experiments is shown in Fig. 4. The anode is composed of two independent single-particle anodes on a single substrate. Each an-

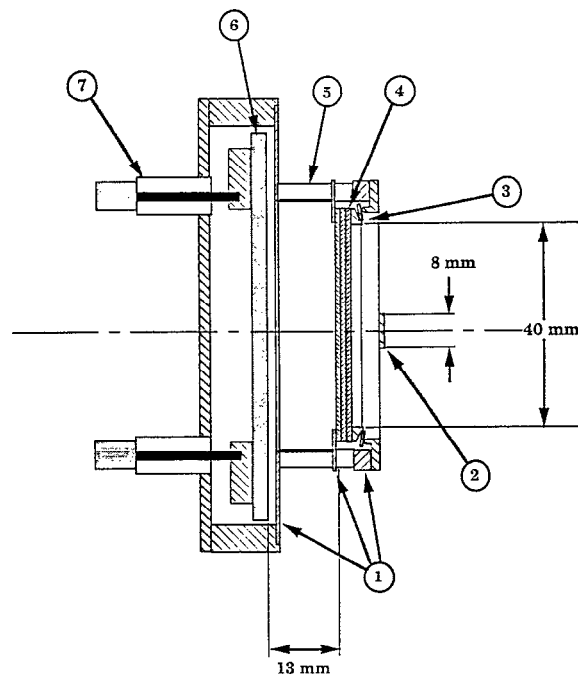


FIG. 5. Schematic of coincidence wedge-and-strip anode detector assembly. (1) kovar/alumina brazed body assembly. (2) 8 mm wide beam block. (3) Spring-loaded ring assembly for holding microchannel plate Z-stack in place. (4) Z-stack of image-quality microchannel plates. (5) Electron drift region with resistive coating (resistance $\approx 4 \text{ G}\Omega$) on the inner wall. (6) Quartz anode substrate with photoetched copper anode. (7) Feedthroughs for output signals. For the detection of neutral particles, the front end of the detector assembly is held at -4.4 kV , giving microchannel plate voltages of $\approx 1300 \text{ V/plate}$, and a drift region voltage of 500 V over 1.3 cm .

ode is composed of three conductors (wedge, strip, and zig-zag), with a ground plane surrounding the entire pattern. The wedges taper linearly along the x -axis while the strips widen linearly along the y -axis. The zig-zag or Z conductor fills up the rest of the active area, allowing normalization of the total charge. The position algorithms for x and y are

$$x \approx \frac{\alpha Q_w - \beta Q_Z}{(Q_w + Q_s + Q_Z)} \quad (5a)$$

and

$$y \approx \frac{\gamma Q_s - \delta Q_Z}{(Q_w + Q_s + Q_Z)} \quad (5b)$$

The small correction factors β and δ compensate for the cross talk between the wedge and strip conductors and the Z -conductor, as discussed by Siegmund⁵⁸ and by Somorjai and co-workers.⁵⁹ The two anodes abut at the innermost wedges, allowing dissociation events with minimal particle recoils to be recorded. The actual pattern used has a period of 0.8 mm , with minimum and maximum wedge fractions of 0.04 and 0.40 and minimum and maximum strip fractions of 0.06 and 0.40 . The insulating gaps between conductors are $40 \mu\text{m}$ wide. The anode is photoetched on a $6 \mu\text{m}$ vapor-deposited Cu layer on a quartz substrate.

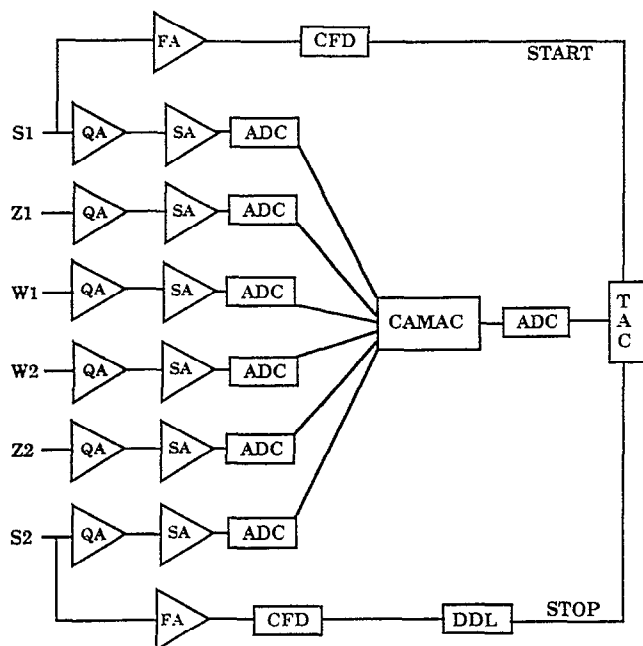


FIG. 6. Schematic of the data acquisition system. W1,S1,Z1 and W2,S2,Z2, charge signals from the two halves of the C-WSA detector; QA, Canberra 2004 charge-sensitive preamplifiers; FA, AC-coupled ComLinear CLC100 fast timing amplifiers used to obtain fast timing pulses from the output of each half of the anode; SA, Ortec 575A spectroscopy amplifiers; ADC, Ortec 413A analog-to-digital converters; TAC, Canberra 2044 time-to-amplitude converter; CFM, Tennelec TC455 constant-fraction discriminator; DDL, Precision Instruments 9650 digital delay generator. The time-to-amplitude converter and analog-to-digital converters are externally gated to accept signal only when photofragments are expected. Calibration of the time-to-amplitude converters indicated that timing resolution of ≈ 0.5 ns is realized with this equipment.

A schematic of the C-WSA particle detector housing is shown in Fig. 5. The detector housing consists of an alumina/kovar microchannel-plate holder assembly, with a resistively coated electron drift region. A Z-stack of three Phillips G12/46-DT 13-13-13 46 mm diameter microchannel plates is used to amplify the secondary electrons produced by the impact of high-energy neutral particles, providing a gain of $\approx 2 \times 10^7$. The narrow pulse height distributions obtained with the Z-stack⁶⁰ allows discrimination of multiple-particle from single-particle events. The detector has an active area diameter of 40.4 mm, but only 34 mm is used due to distortions near the outer perimeter inherent in the present detector housing design.

To record the time and position information for each pair of coincident photofragments, commercial nuclear instrumentation equipment is used. A schematic of the data acquisition system is shown in Fig. 6. After each dissociation laser pulse, the analog-to-digital converters are checked for wedge, strip, Z, and time-to-amplitude converter signals corresponding to particle impacts and the raw x , y , and coincidence time data are saved. The raw data are subsequently converted to center-of-mass kinetic energy release, angular, and mass distributions by implementing the position algorithm [Eq. (5)] and the kinematic equations (1)–(3). False coincidences are elimi-

nated as previously described and valid coincident events are binned into the appropriate distributions of interest, i.e., mass, kinetic energy, and angular distributions. The processing of these raw distributions, $\mathcal{S}(E_T, \theta)$, is discussed in Sec. IV A.

Initial characterization of the C-WSA particle detector was done by covering the first microchannel plate with a pinhole-pattern array photoetched onto a 0.002 in. Ni sheet (Stork-Veco Corp.) and illuminating with a low intensity mercury lamp.⁵⁸ This sheet contained 50 and 25 μm pinholes in a 4×2 mm period rectangular array. The factors used in the position algorithms in Eqs. (5) were then adjusted to get the best-fit between the observed two-dimensional image and the known positions of the pinholes. Analysis of the intensity profiles of the imaged pinholes indicate that the spatial resolution is on the order of 75 μm full-width-at-half-maximum in y and 130 μm in x . This calibration also showed that an 8 mm wide beam block was needed to prevent significant spill-over of signal near the center-line onto the adjacent half of the detector. The factors obtained by this procedure were further refined by calibration using the O₂ photodissociation results discussed below. From these calibration procedures, it was determined that the usable active detector area in these experiments was between azimuthal (ϕ) angles of 35° and 145° on each half of the detector and with maximum single-particle recoil distances of 17 mm or less.

III. RESULTS

A. O₂

The Schumann–Runge absorption bands of O₂ involve the $B^3\Sigma_u^- \leftarrow X^3\Sigma_g^-$ electronic transition and cover a wide range of wavelengths due to a large change in equilibrium bond length and a weak force constant in the B state.⁵⁰ It has long been known that the B state rapidly predissociates, and numerous experimental and theoretical studies of the predissociation mechanism have been carried out to obtain an accurate picture of the UV photophysics of this extremely important molecule.^{61–65} Because the O₂ bond energy of 5.117 eV is well known,⁶⁶ this system provides an independent check of the detector performance. Minor uncertainties arise in using O₂ as a calibrant, however, due to the unknown spin–orbit state distribution of the pair of 3P_J O atoms produced by predissociation from the O₂ $B^3\Sigma_u^-$ state.

The $v=0$ level of the O₂ $X^3\Sigma_g^-$ state has very poor Franck–Condon overlap with the predissociating levels of the $B^3\Sigma_u^-$ state, while transitions from the $v=0$ level to the repulsive region of the B state potential energy curve are beyond the range of our dissociation laser ($\lambda_{\text{min}}=208$ nm). In contrast, the excited vibrational levels of the X state have much better overlap with the lower-lying predissociating levels of the B state. Fortunately, photodetachment of O₂⁻ is a convenient way of generating vibrationally excited O₂, as previously discussed.⁴⁹ This allows us to excite the O₂ $B^3\Sigma_u^-(v'=7) \leftarrow X^3\Sigma_g^-(v''=4)$ transition at 210.23 nm which has a relatively favorable Franck–Condon factor ($q_{v'v''}=0.031$).⁶⁷ A photodissociation cross

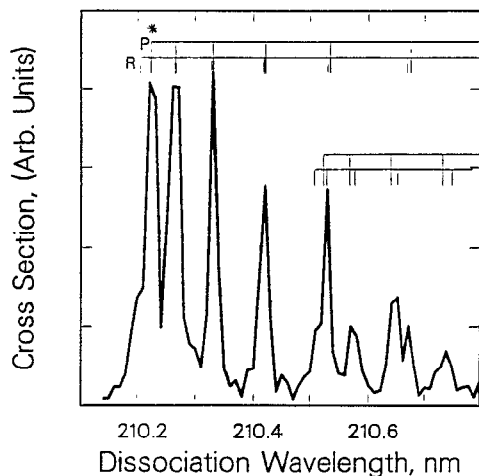


FIG. 7. Total cross section scan of the predissociation of O₂ $B^3\Sigma_u^- v=7$ and 10. The upper comb denotes the $v'=7 \leftarrow v''=4$ transitions. The overlapping $R(3)$ and $P(1)$ lines used in the dissociation experiment are marked with an asterisk. The lower comb denotes the weaker $v'=10 \leftarrow v''=5$ transitions.

section spectrum of this region, including the weaker $v'=10 \leftarrow v''=5$ transition, is shown in Fig. 7. This spectrum shows the characteristic rotational structure of the Schumann–Runge band; the R branch head is at the origin, and the R branch is strongly degraded to the red, overlapping the P branch lines. The assignment of the transitions was made using the constants of Creek and Nicholls.⁶⁸

Figures 8 and 9 show the KER spectrum and angular distribution obtained by exciting the overlapping $R(3), P(1)$ lines in the $B(v'=7) \leftarrow X(v''=4)$ band. The ion beam energy was 8 keV. For now, we will focus on the KER spectrum; the angular distribution will be discussed in Sec. IV A. The peak in the KER spectrum at 1.523 eV

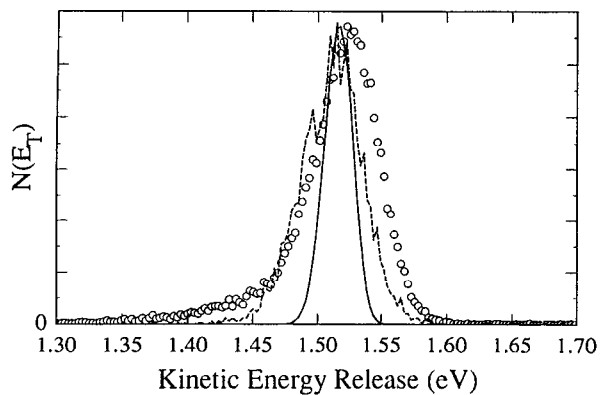


FIG. 8. O₂ → O + O KER spectrum recorded at a beam energy of 8 keV at a dissociation wavelength of 210.23 nm. The open circles are the experimental results integrated over the usable portion of the detector face, with the Monte Carlo simulation given by the solid line. The dotted line curve shows the experimental results from a 4 mm wide vertical stripe at the center of the detector, scaled by the number of events in this stripe relative to the total number of events. Note that this removes the long low-energy tail from the data.

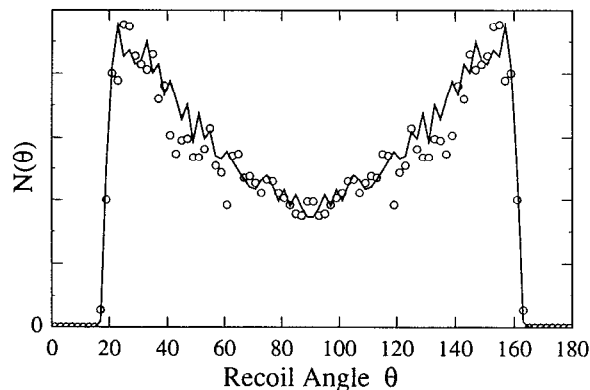


FIG. 9. Angular distribution of the O atom fragments at 210.23 nm, restricted to a 4 mm wide vertical strip at the center of the detector. The raw data are shown as open circles, and the Monte Carlo simulation with $\beta=0.7$ is given by the solid line.

has a full-width-at-half-maximum (FWHM) of 59 meV. This width is determined by several factors: primary beam energy spread, position and time resolution, residual nonlinearities in the position and time data, and, finally, the dynamics of the predissociation of O₂. The primary beam energy spread is dominated by the axial compression scheme used to optimize the overlap of the ion packet with the detachment and dissociation lasers. For O₂ at 8 keV, this amounts to ≈ 70 eV FWHM, giving a spread in the measured KER of $\Delta E_{\text{cm}}/E_{\text{cm}} \approx \Delta E_0/E_0 = 0.9\%$. The spatial resolution quoted earlier produces an uncertainty of $\Delta E_{\text{cm}}/E_{\text{cm}} \approx 2\Delta R/R_{\text{max}} = 0.8\%$.¹⁷ The timing resolution of 0.5 ns contributes a similar error for those recoils that lie along the beam axis. Adding these relative errors in quadrature gives $\Delta E_{\text{cm}}/E_{\text{cm}} \approx 1.2\%$, or an expected resolution of ≈ 18 meV. The angular resolution is primarily determined by the energy spread of the beam and the accuracy with which time and position can be measured since the beam is so highly collimated. Propagation of random errors through Eq. (1) indicates that $\Delta\theta \approx 0.5^\circ$ is easily achievable.

Some of the discrepancy between the observed width of the KER spectrum and the expected value of 18 meV is due to residual nonlinearities in the position measurement. The low energy tail on the KER spectrum (open circles in Fig. 8) is an example of these nonlinearities. In principle, such a KER distribution could be due to dissociation of an excited state with a several hundred ns lifetime. However, by selecting a 4 mm wide vertical strip near the center of the detector, where the nonlinearities are minimized, we find that the low energy tail disappears, the energy spread drops to 50 meV FWHM, and the peak of the KER spectrum is shifted to 1.515 eV. This is shown by the dashed line in Fig. 8. Thus, the low energy tail is due to imperfect operation of the detector. We believe it is due to photodissociation events in which both fragments strike the detector near the beam block. In such a case, charge spillover between the two halves of the detector is large enough so that the measured distance between the O atoms is too small, resulting in an artificially low kinetic energy release.

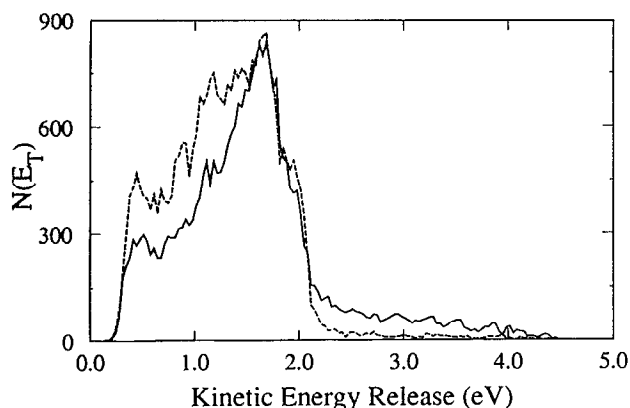


FIG. 10. Raw N₃→N+N₂ KER spectra for N₃. The solid line shows the results obtained when the (000) level of the \tilde{B} state is pumped, while the dashed line shows the (010) spectrum.

This charge spillover effect is most important for equal mass fragments, since this results in a larger number of events in which both fragments land near the beam block.

We also must consider the influence of the predissociation dynamics of O₂ on the observed KERs. As seen in Fig. 7, the $R(3)$ and $P(1)$ rotational transitions overlap. This effect on the energy resolution is negligible, however, as the $J=0$ to $J=4$ spacing in the $\tilde{B}^3\Sigma_u^-$ state is only 2 meV. However, the O atom spin-orbit state distribution may have a large effect, with a maximum possible spread of 56 meV when either two O(³P₂) or O(³P₀) atoms are produced. The peak KER value obtained experimentally is 1.515 eV, which matches the O(³P₂)+O(³P₁) limit. In recent higher resolution measurements in our laboratory, the O₂ KER showed several partially resolved peaks, indicating that a substantial fraction of the energy spread in Fig. 8 is from the O atom spin-orbit distribution. This more recent work will be discussed in a future publication;⁶⁹ the relevant implication is that the resolution in the current study is better than 40 meV.

B. N₃

In our continuing study of N₃ photodissociation dynamics, we have recorded kinetic-energy and angular distributions at 271.9, 270.9, and 270.2 nm (*in vacuo*). The first two wavelengths are transitions within the $\tilde{B}^2\Sigma_u^+ \leftarrow \tilde{X}^2\Pi_g$ band. They correspond²⁹ to the $^2\Sigma_u^+(000) \leftarrow ^2\Pi_{g,3/2}(000)$ electronic origin and the $^2\Pi(010) \leftarrow ^2\Sigma^+(010)$ vibronic sequence band, respectively, where $v_1v_2v_3$ notation is used. The third wavelength corresponds to an unassigned transition which may also be in the $\tilde{B} \leftarrow \tilde{X}$ band. The raw kinetic energy distributions obtained at 271.9 and 270.9 nm are shown in Fig. 10. These spectra consist of 60 000–80 000 coincidence events and are acquired in several hours each. Preliminary results at 270.2 nm (not shown) are very similar to the 270.9 nm results.

A qualitative assessment of the important channels in the dissociation of the $\tilde{B}^2\Sigma_u^+$ state can be immediately reached on the examination of Fig. 10. The most promi-

nent feature in both bands is the large peak centered between 1 and 2 eV, consistent with N(²D) production (see Fig. 1). This feature has an apparent threshold of ≈ 2.2 eV, which indicates that the N₃ is approximately thermoneutral relative to N+N₂. The electronic origin KER spectrum, however, has a significant pedestal extending out to ≈ 4.6 eV. Given what is known about the energetics of N₃, the only possible explanation of this pedestal is that the spin-forbidden dissociation producing N(⁴S)+N₂ is occurring appreciably from the N₃ $\tilde{B}^2\Sigma_u^+(000)$ state. The spin-forbidden channel is also seen for the (010) band, but, in a striking mode-specific effect, it is markedly reduced in intensity. There is also evidence for a shoulder on the low energy side in both bands, with an onset of ≈ 0.75 eV; at this energy, the N(²P) channel is accessible. To convert the raw KER spectra and angular distributions to true center-of-mass distributions requires further data analysis, as discussed in the next section.

IV. ANALYSIS

The quantities of interest in a photodissociation dynamics experiment are the true photofragment center-of-mass kinetic energy and angular distributions. As shown in many earlier studies,^{2,4} these dynamical observables can provide clear insights into the detailed photodissociation mechanism. The kinetic energy distribution can reveal the forces at work during the dissociation, and in cases where internal states of the products are resolved, yield the detailed energy disposal. The anisotropy of the photofragment angular distribution provides information about the symmetry of the dipole transition, coupled with the dynamics of the dissociation. For one-photon dissociation, the form of the photofragment energy and angular distribution $\mathcal{P}(E_T, \theta)$ can be written as⁷⁰

$$\mathcal{P}(E_T, \theta) = P(E_T) [1 + \beta(E_T) P_2(\cos \theta)], \quad (6)$$

where θ is the angle between the photofragment recoil vector and the electric vector of the dissociation laser, $P_2(\cos \theta)$ is the second Legendre polynomial, $\beta(E_T)$ is the (energy-dependent) anisotropy parameter, and $P(E_T)$ is the angle-integrated kinetic energy distribution. The anisotropy parameter β can range from +2 (corresponding to a $\cos^2 \theta$ photofragment angular distribution) to -1 (for a $\sin^2 \theta$ distribution).⁷⁰ The functions $P(E_T)$ and $\beta(E_T)$ represent completely the information that can be distilled from the raw data in a photofragment translational spectroscopy experiment. In this section, we describe how the $P(E_T)$ and $\beta(E_T)$ are determined in our experiments on O₂ and N₃.

A. Detector acceptance analysis

Because our detector has both a finite size and a beam block across its center, some of the photodissociation events cannot be detected in coincidence, especially when unequal mass fragments are produced. For each photodissociation event, both fragments must strike the active area of the detector in order to be recorded as a coincidence event. For example, both fragments must have sufficient recoil velocity perpendicular to the beam block (along the

y-coordinate in Fig. 3) to clear the 4 mm halfwidth of the beam block. For the photodissociation of an 8 keV beam of N₃, this requirement prevents the observation of *any* fragmentation events with <0.20 eV kinetic energy. In addition, the fragments must not recoil out of the field-of-view of the detector, which in this experiment was defined by a radius of 17.0 mm. In the N₃ case, the onset of the field-of-view cutoff occurs for events with purely transverse recoil ($\theta=90^\circ$ in Fig. 3) at 1.15 eV kinetic energy release. While the detector is sensitive to recoils with much higher kinetic energy release than 1.15 eV, the polar angular acceptance of the detector goes down with increasing recoil energy. Thus, the kinetic energy and angular distributions measured in the laboratory for N₃ photodissociation will be strongly influenced by the detector acceptance. We must accurately model the detector acceptance to determine the kinetic energy and angular distribution $\mathcal{P}(E_T, \theta)$ from the raw data. Fortunately, this purely geometric problem can be solved in a quite straightforward manner.

We have taken two independent approaches to this problem. The first approach, which we have used previously, is that of Monte Carlo forward convolution.^{16,71} The second approach, which we present here for the first time, involves a direct inversion of the raw data into the desired quantities $P(E_T)$ and $\beta(E_T)$.

In our Monte Carlo simulations, trial input center-of-mass kinetic energy and angular distributions [$P(E_T)$ and $\beta(E_T)$ of Eq. (6)] are input and averaged over all of the apparatus parameters, such as beam angular and velocity distributions, finite interaction volumes, resolution of the time and position measurements, and the active area of the two-particle detector. We have incorporated all of the important sources of experimental broadening with the exception of nonlinearities in the position measurement, which are most significant for equal mass fragments integrated over the full active area of the detector face. Application of this algorithm to the case of O₂ predissociation is simple—in the absence of O atom spin-orbit-state resolution, a single value for the kinetic energy release E_T and anisotropy parameter β is sought which fits the data. The solid line in Fig. 8 is a Monte Carlo simulation of the O atom data for a 4 mm wide vertical strip on the detector face, assuming production of O(³P₂) + O(³P₁) atoms. The simulation is considerably narrower than the data from the 4 mm strip, but, as mentioned above, recent results show that much of this discrepancy is in fact due to the spin-orbit state distribution of the O atoms. The O atom angular distribution shown in Fig. 9 is fit well by the Monte Carlo simulation assuming a value of $\beta=0.7$ for the anisotropy parameter. This degree of anisotropy is consistent with the parallel ($\Delta\Lambda=0$) electronic transition taken together with the 3 ps excited state lifetime,⁷² which is roughly equal to the O₂ B ³Σ_u⁻ rotational period.

Application of the Monte Carlo forward convolution technique to N₃ is more problematic, as in this case there are many product channels open, and the detector acceptance is affected by both the energy and angular distributions of the products. The Monte Carlo technique has no difficulty simulating this situation—the only question is to

find the correct input distributions $P(E_T)$ and $\beta(E_T)$ by trial and error, a tedious process at best.

As a preferred alternative, we have numerically modeled the energy and angular dependence of the detector acceptance, providing unbiased center-of-mass kinetic energy and angular distributions. This direct inversion approach is similar in spirit to a more approximate one previously implemented by Los and co-workers.¹⁹ Their treatment of dissociative charge-exchange processes assumed isotropic product angular distributions [$\beta(E_T)=0$ for all E_T]*—*a simplifying assumption that cannot be made in our case, as angular anisotropy is expected in photodissociation processes. The numerical algorithm we have developed allows the direct extraction of the quantitative center-of-mass kinetic energy and angular distributions [$P(E_T)$ and $\beta(E_T)$] as described below.

The raw data, consisting of 60 000–80 000 valid coincidence events, are binned into a two-dimensional raw energy-angle array $\mathcal{S}(E_T, \theta)$ with the aid of Eqs. (1) and (2). In order to convert $\mathcal{S}(E_T, \theta)$ into the desired joint probability distribution $\mathcal{P}(E_T, \theta)$ as it appears in Eq. (6), we must determine the acceptance of the detector for each value of E_T and θ . We define the detector acceptance function $\mathcal{D}(E_T, \theta)$ such that

$$\mathcal{P}(E_T, \theta) = \mathcal{S}(E_T, \theta) / \mathcal{D}(E_T, \theta). \quad (7)$$

This function $\mathcal{D}(E_T, \theta)$ is the probability of observation of a coincidence event with given values of kinetic energy release E_T and recoil angle θ . The photofragment angular distribution is azimuthally symmetric about the electric field vector **E** of the dissociation laser (which is parallel to the ion beam axis in these experiments), so $\mathcal{D}(E_T, \theta)$ is found by determining the range of azimuthal angles over which both fragments strike the active area of the detector. More specifically,

$$\mathcal{D}(E_T, \theta) = \frac{1}{2\pi} \int_0^{2\pi} D(E_T, \theta, \phi) d\phi. \quad (8)$$

Here, $D(E_T, \theta, \phi)$ is the doubly-differential detector acceptance function which gives the probability of detection of a dissociation event with kinetic energy release E_T and recoil angles θ and ϕ . Neglecting the finite size of the radical beam (considered below), $D(E_T, \theta, \phi)$ is either 0 or 1. For specific values of E_T , θ , and the fragment masses, it is elementary to determine the range of ϕ values for which $D(E_T, \theta, \phi)=1$. As an example, consider our N₃ experiment. For an energy release of 1.7 eV (at the peak of the raw data distributions shown in Fig. 10), and polar recoil angle of $\theta=40^\circ$, $D(E_T, \theta, \phi)=1$ for $39^\circ < \phi < 141^\circ$ and for $219^\circ < \phi < 321^\circ$. $D(E_T, \theta, \phi)=0$ for other values of ϕ , for which the beam block prevents observation of the slower N₂ fragment. Thus, we have $\mathcal{D}(E_T=1.7 \text{ eV}, \theta=40^\circ) = 2(102^\circ)/360^\circ = 0.567$.

Once $\mathcal{D}(E_T, \theta)$ is determined, the raw energy and angular distributions $\mathcal{S}(E_T, \theta)$ can be converted directly into the (unnormalized) probability distribution $\mathcal{P}(E_T, \theta)$ via Eq. (7). Then, for each kinetic energy interval ($E_i - \Delta E/2, E_i + \Delta E/2$), we directly determine the anisotropy parameter $\beta(E_T)$ by a simple least squares fit to

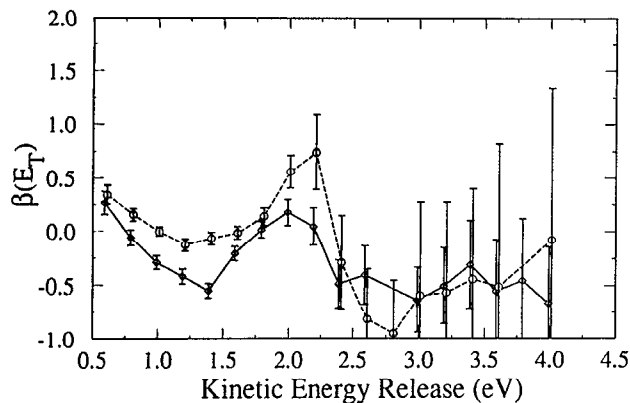


FIG. 11. The anisotropy parameter $\beta(E_T)$ for N₃ found by the direct inversion technique (see text). The solid line with diamonds shows the results for the (000) band, and the dashed line with circles shows the (010) results. The error bars shown are 1σ standard uncertainties from the least-squares fit to Eq. (6).

Eq. (6). Application of this algorithm to the O₂ data, for which only a single value of β is needed, yields $\beta=0.70 \pm 0.05$, in perfect agreement with that found by the Monte Carlo forward convolution. In the case of N₃ photodissociation, Fig. 11 shows the resulting $\beta(E_T)$ obtained in our experiment. These results were obtained using energy intervals of $\Delta E=0.4$ eV in the kinetic energy release, centered at the points shown. This ability to extract an energy-dependent $\beta(E_T)$ directly from the raw data is a powerful advantage of acquiring simultaneous energy and angular distributions; the energy dependence of β is typically not obtained from conventional mass-spectrometric photofragmentation studies, although it can be in some cases.⁷³

The final step in the direct inversion analysis is to find the angle-integrated kinetic energy distribution $P(E_T)$ at the highest energy resolution. Using the appropriate values of $\beta(E_T)$ obtained above, we determine $P(E_T)$ for energy intervals of 0.033 eV in width, i.e., intervals that are comparable to the instrumental energy resolution. The kinetic energy distributions are shown in Fig. 12 for the two vibronic bands (000) and (010). The plots in Figs. 11 and 12 represent the main result of this work.

As an independent check on the results obtained by the detector acceptance analysis, the deduced $P(E_T)$ and $\beta(E_T)$ distributions can be entered as trial inputs into a Monte Carlo simulation. This comparison is shown in Fig. 13 for the KER and angular distributions obtained for the (000) band. The agreement between the raw data and the Monte Carlo simulation using these inputs is excellent, and gives an important check on the consistency of these two very different data analysis algorithms. The agreement between the two algorithms was improved significantly when we accounted for the size and shape of the radical beam in the calculation of the doubly-differential acceptance function $D(E_T, \theta, \phi)$. The results shown in Figs. 11 and 12 were obtained after we modeled the beam profile at the detector as a two-dimensional Gaussian with a 1 mm FWHM. After this improvement, $D(E_T, \theta, \phi)$ took values between 0

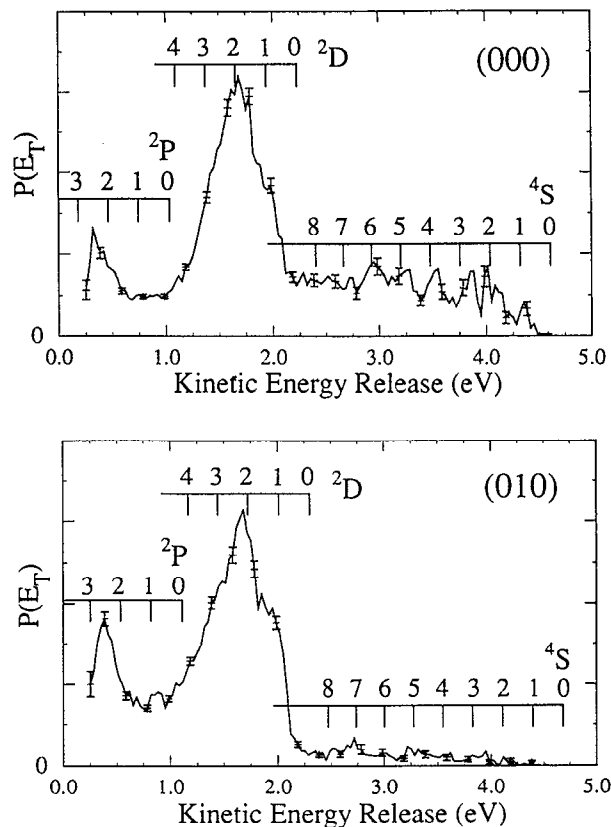


FIG. 12. Center-of-mass translational energy distributions $P(E_T)$ found by the direct inversion technique. Every sixth point shows the 1σ error from counting statistics. The combs show the origins of the accessible N+N₂(*v*) vibrational levels.

and 1, representing what *fraction* of the radical beam profile gives rise to coincidences for kinetic energy release E_T and recoil angles θ and ϕ . The most significant discrepancy remaining between the two methods is for the smallest energy releases, where the direct analysis has difficulty calculating the very small acceptance of the detector. This is probably due to the fact that the direct inversion does not take into account the velocity distribution and the angular divergence of the radical beam. The overall agreement between the data and the Monte Carlo simulation indicates, however, that it would not be meaningful to improve the fit to the data by adjusting the $P(E_T)$ and $\beta(E_T)$ distributions determined in the detector acceptance analysis.

There are two major sources of uncertainty in the $P(E_T)$ plotted in Fig. 12. One is simply the statistical noise associated with the Poisson statistics inherent in a counting experiment. This uncertainty, shown as 1σ error bars in Fig. 12, is well estimated by the square root of the number of counts in a given 0.033 eV energy bin. The statistical uncertainty is uncorrelated from one point to the next. The second source is associated with the uncertainty in $\beta(E_T)$ used in the last step of the analysis [see Fig. 11 for the standard error in $\beta(E_T)$ deduced in the linear least-squares fit]. This error is negligible in some parts of the kinetic energy release spectrum, and dominates in others. The $\beta(E_T)$ uncertainty is especially important at high E_T

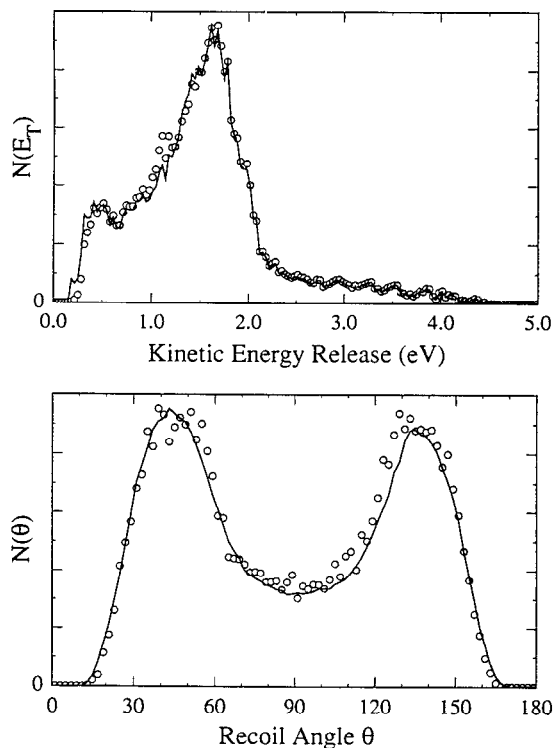


FIG. 13. Raw $N_3 \rightarrow N+N_2$ KER and angular distributions for the (000) band (shown as circles) compared to the results of a Monte Carlo forward convolution simulation (solid lines), using the $P(E_T)$ and $\beta(E_T)$ in Figs. 12 and 11, respectively.

(>2.0 eV) where the polar angular acceptance becomes small. The uncertainty in $\beta(E_T)$ is locally correlated in the energy release spectrum, so we do not present this error added in quadrature to the statistical error; further consideration of the $\beta(E_T)$ uncertainty is discussed in Sec. IV B.

B. Branching ratio analysis

Having obtained the true center-of-mass $P(E_T)$ distributions, we can address the question of the energetics and energy disposal in the photodissociation of N_3 . For both bands, the energy distributions show evidence for N_2 product vibrational-state resolution, as indicated by the combs in Fig. 12, with this structure being most noticeable in the $N(^4S)$ region of the (000) spectrum. We have determined that the energy resolution of the detector is better than 40 meV, considerably smaller than the N_2 vibrational frequency (290 meV). Hence, the observation of only partially resolved vibrational structure indicates that there is significant rotational excitation of the N_2 products. The most striking effect noticed in these $P(E_T)$ plots was already noted in the examination of the raw data; the branching ratio for $N(^4S)$ production drops significantly (by a factor of 6) when one quantum of the bend in the upper N_3 state is excited. In addition, the significance of the low energy shoulder on the raw KER spectra, which is most likely due to a $N(^2P)+N_2$ dissociation channel is now seen distinctly as a peak in $P(E_T)$ below 0.7 eV in both spectra.

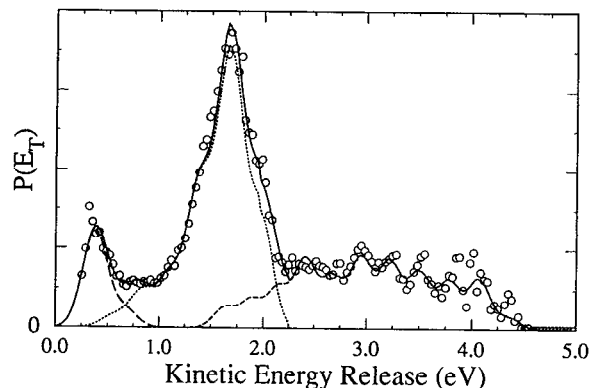


FIG. 14. Simulation of $P(E_T)$ for the (000) band using the $N+N_2$ internal energy distribution in Table I. For each $N(^4S, ^2D, ^2P)+N_2(v)$ limit, the model rotational distribution is as described in the text. The contributions from each of the electronic branches are drawn separately below the data (open circles); the dashed line represents the $N(^4S)$ limit, the dotted line $N(^2D)$, and the long-dashed line $N(^2P)$.

The energy disposal and branching ratios for the products of N_3 dissociation can be assessed by decomposition of the $P(E_T)$'s into plausible electronic, vibrational and rotational distributions of the $N+N_2$ products. We have done this by fitting the $P(E_T)$'s with Gaussian rotational energy distributions for each $N+N_2(v)$ channel accessible. These Gaussian distributions have a constant width throughout the vibrational progression belonging to each electronic state; in addition, the Gaussian distributions have a common offset between their peaks and the vibrational origins ($J=0$) throughout the manifold belonging to each electronic state. The Gaussians are truncated at the origin of the vibrational bands. In the absence of well-resolved vibrational structure, this decomposition is far from unique, especially where there is overlap between vibrational manifolds belonging to different N atom electronic states. However, in the $N(^4S)$ region of the (000) band and the $N(^2D)$ region of the (000) and (010) bands, there is enough vibrational resolution that the fits are well determined in these regions.

In addition to the parameters that describe the Gaussian distributions, the fits required a value for the bond dissociation energy $D_0(N_2-N)$. The $P(E_T)$'s for the (000) and (010) bands were fit best when $D_0 = -0.05 \pm 0.10$ eV. From this value, the 0 and 298 K heats of formation of N_3 are $\Delta H_{f,0}^0(N_3) = 113.7 \pm 2.3$ kcal/mol and $\Delta H_{f,298}^0(N_3) = 112.8 \pm 2.3$ kcal/mol.³³ These values agree very well with the earlier experimental determination by Brauman and co-workers,³⁰ and are also consistent with the recent *ab initio* study of Martin *et al.*³⁴

The best fit to the (000) band, using $D_0 = -0.05$ eV, is shown in Fig. 14. In the $N(^4S)$ manifold of the (000) band, the rotational energy distributions are represented as Gaussians with a FWHM of 0.25 eV, peaking at 0.25 eV above the $J=0$ origin ($J_{\text{peak}} \approx 32$). For $N(^2D)$, the Gaussians have a FWHM of 0.28 eV, offset by 0.26 eV from the origin. For $N(^2P)$, the best fit was given by a hotter rotational distribution; the Gaussians have a FWHM of 0.28

TABLE I. Product branching ratios for the N+N₂ products following the predissociation of the (000) and (010) levels of the $\tilde{B}^2\Sigma_u^+$ state of N₃, using the fitting procedure discussed in the text. The fit results are also shown in Fig. 14. The electronic branching ratios are given relative to the N(²D) intensity. The uncertainties in the N(⁴S) channel branching ratios are the result of the large uncertainty in $\beta(E_T)$ for $E_T > 2.5$ eV (see Fig. 11). The uncertainties in the N(²P) channel, on the other hand, reflect the acceptance cutoff at 0.20 eV, and also the ambiguity caused by overlap with the N(²D)+N₂(ν) manifold. The vibrational distribution in each channel is normalized to unity. The intensities of the vibrational levels marked with a dagger (†) were fixed in the least-squares fit. The Franck–Condon vibrational distribution (FCF) is also noted for reference, as discussed in the text.

	Branching ratio	$\nu=0$	$\nu=1$	$\nu=2$	$\nu=3$	$\nu=4$	$\nu=5$	$\nu=6$	$\nu=7$	$\nu=8$	$\nu=9$	$\nu=10$
000	⁴ S	0.73 ^{+0.31} _{-0.14}	0.03	0.10	0.09	0.11	0.13	0.14	0.10	0.13	0.08 [†]	0.06 [†]
	² D	1	0.18	0.43	0.23	0.08	0.06	0.02 [†]				
	² P	0.18 ^{+0.18} _{-0.09}	0.16	0.84								
010	⁴ S	0.12 ^{+0.07} _{-0.04}	0.01	0.03	0.10	0.09	0.17	0.10	0.21	0.15	0.09 [†]	0.04 [†]
	² D	1	0.20	0.36	0.22	0.11	0.08	0.03 [†]				
	² P	0.22 ^{+0.22} _{-0.11}	0.12	0.88								
FCF		0.23	0.29	0.23	0.14	0.07	0.03	0.01

eV, offset by 0.37 eV from the origin ($J_{\text{peak}} \approx 39$). This offset for N(²P) production is large enough that the vibrational assignment for the peak in $P(E_T)$ is somewhat ambiguous; we have assigned it to the N(²P)+N₂($\nu=1$) limit, but it could feasibly be assigned to $\nu=2$, with a 0.09 eV offset. For the (010) band, the FWHM of the Gaussian distributions are essentially the same, but the offsets are increased by 60–90 meV. This additional offset can be explained by the fairly direct transfer of the 57 meV of bend excitation present in the N₃ $\tilde{B}^2\Sigma_u^+$ (010) level into N₂ product rotation.

The vibrational distributions and electronic branching ratios derived from these fits are listed in Table I, along with upper and lower limits for the electronic branching ratios found by fitting the $P(E_T)$ distributions obtained with the upper and lower limits to $\beta(E_T)$ shown in Fig. 11. These results show that the N(⁴S) branching ratio has a large uncertainty due to the difficulty of measuring β for high energy releases. It also must be noted that to calculate the N atom branching ratios, we have assumed that the bands overlap in the manner shown in Fig. 14. Also shown in Table I is the Franck–Condon vibrational distribution in N₂ that would result from a sudden bond length change from 1.18 Å [r_e in N₃ (Ref. 29)] to 1.10 Å [r_e in N₂ (Ref. 74)]. The vibrational distribution in the N(⁴S) channel is very hot, while the N(²D) channel vibrational distribution peaks at $\nu=1$ in both the (000) and (010) bands, similar to the Franck–Condon distribution. Production of N(²P) provides the most likely explanation for the peak in $P(E_T)$ below 0.7 eV. However, the precise determination of the N(²P) branching ratio is problematic due to the overlap with the products correlated to N(²D) atom production.

The error bars in our value for D_0 largely result from the correlation between the bond dissociation energy and the offsets used in the rotational energy distributions. There is no guarantee that our KER spectra contain a measurable amount of signal for N(⁴S)+N₂($\nu=0, J=0$), especially in light of the considerable rotational excitation of the N₂ fragment. Thus, the positions of the true $J=0$

rotational origins (and therefore the bond dissociation energy D_0) could only be determined to an accuracy of 0.10 eV. On the other hand, the highest observed kinetic energy release can be determined quite precisely; as a result, an upper bound on D_0 can be determined with higher precision than D_0 itself. Examination of the data in the (000) band shows that the maximum KER is recorded in the 0.033 eV wide energy bin centered at 4.550 eV, so events with an observed KER ≥ 4.533 eV were recorded. Taking into account the kinetic energy resolution of < 0.040 eV FWHM, the best estimate for the lower limit to the maximum KER is 4.513 eV. In these measurements, the photodissociation laser linewidth overlaps several N₃ rotational transitions, and rotational levels with $N \approx 10$ may contribute 0.007 eV to the maximum energy release. With all of these points considered, we deduce an *upper limit* to the bond dissociation energy, $D_0 \leq 0.05$ eV ± 0.03 eV. Thus, we find that N₃ is at most slightly stable relative to N(⁴S)+N₂. This upper bound is quite consistent with the bond dissociation energy $D_0 = -0.05 \pm 0.10$ eV determined by the fitting procedure described above.

V. DISCUSSION

The new C-WSA particle detector coupled with fast radical beam photodissociation spectroscopy allows detailed photofragment kinetic energy, mass and angular distributions to be obtained for well-characterized free radicals. The experiments discussed have shown that N₃ dissociates by both spin-allowed and spin-forbidden processes, as previously seen in the case of NCO and N₂O⁺. The salient difference noted between N₃ and NCO dissociation is that in the case of NCO, once the spin-allowed N(²D) products become energetically allowed, they rapidly dominate the product branching ratio. For N₃, however, both low-lying doublet states of the N atom and the N(⁴S) ground state are accessible from all levels of the $\tilde{B}^2\Sigma_u^+$ state, yet there is a large change in the (²D):(sup>4S) branching ratio with the addition of one quantum of bend-

ing excitation. This is a clear example of mode-specific dissociation dynamics, in which the final product state distribution can be dramatically affected depending on which level of the predissociating state is prepared. Another significant result from this work is the high level of N₂ rotational excitation in both the spin-forbidden and spin-allowed channels, even though the N₃ \tilde{B} state is linear. This implies that bent geometries of N₃ participate in dissociation from the \tilde{B} state.

These experiments have also independently confirmed that N₃ is slightly unstable relative to N(⁴S) + N₂ at 0 K ($D_0 = -0.05 \pm 0.10$ eV), in good agreement with Brauman and co-workers.³⁰ The energetics of the N₃ system are shown in Fig. 1. The current experiments are profoundly direct measurements, which do not require any auxiliary thermochemical information. The recent *ab initio* study by Martin *et al.*³⁴ indicates that N₃ is somewhat more stable than this experimental determination, as mentioned in the introduction. However, their calculation is consistent with the upper bound for D_0 determined by this study.

An interesting observation concerns the $P(E_T)$ in the N(⁴S) channel. At higher translational energies, structure which appears to be consistent with resolved N₂ vibrational states is observed. At lower kinetic energies ($2.2 \text{ eV} < E_T < 2.8 \text{ eV}$), however, this structure washes out, implying that rotational excitation *increases* with vibrational excitation. While this nonstatistical behavior may seem counter-intuitive, similar effects have been previously observed by Zare and co-workers in the photodissociation of ICN.⁷⁵ In the case of the nonadiabatic dissociation of ICN, this effect was attributed to the rotational distribution being determined by a geometry change in the excited state prior to dissociation, with the vibrational distribution independently determined by exit-channel interactions. To reach spin-forbidden N(⁴S) + N₂ products, a multistep dissociation mechanism is likely, as discussed below, and similar phenomena may be governing the partitioning of energy in this system as well. In our study, this can only be a qualitative conclusion, as we have not measured precise rovibrational state distributions.

The $\beta(E_T)$ curves in Fig. 11 are also of interest. These plots show a significant energy dependence for β within each band. Although β is not as well determined for $E_T > 2.5$ eV, the N(²D) + N₂ products ($E_T < 2.2$ eV) have a more positive value of β than the N(⁴S) + N₂ products in both the (000) and (010) bands. Moreover, β varies significantly over the energy range where the spin-allowed channels dominate, $0.6 < E_T < 2.2$ eV. In the (000) band, β varies from +0.2 to -0.5 over this range, and in the (010) band, it varies from 0.6 to -0.1. It is somewhat surprising that a positive value of β is observed at all in the photodissociation of the N₃ $\tilde{B}^2\Sigma_u^+$ state, since this state is prepared via a perpendicular electronic transition from the $\tilde{X}^2\Pi_g$ state. However, a geometry change in the molecule prior to dissociation can create a different photofragment anisotropy than that expected for a linear molecule undergoing purely axial recoil.⁷⁸ If the molecule bends significantly from the prepared linear excited state, for example, more transverse recoil is expected, which in our case will

lead to a more positive anisotropy parameter. The differences between the (000) and (010) band $\beta(E_T)$ curves are consistent with this interpretation. $\beta(E_T)$ is consistently more positive as might be expected from a more transverse recoil due to bending excitation. Similar effects have previously been observed in studies of ICN by Zare and co-workers⁷⁵ and HCO by Kable *et al.*⁷⁶

The variation of β for $E_T < 2.2$ eV, may be a further indication of the importance of coupling between the geometry of the dissociating molecule and the photofragment energy distribution. Energy dependent anisotropies have been observed in the statistical decomposition of ionic clusters,⁷⁷ but those experiments have little bearing on the N₃ results. In any case, the anisotropy parameter results offer further support for the idea, implied by the N₂ rotational distributions, that bent geometries play a role in the dissociation of N₃.

The range of $\beta(E_T)$ in Fig. 11 is somewhat inconsistent with the study by Haas and Gericke,²⁶ who estimated a lifetime of at least 370 ps in the (000) band from high-resolution laser-induced fluorescence data. This is considerably longer than the N₃ rotational period (7.6 ps for $J=5$). For complete rotational averaging of a linear molecule, β is reduced by a factor of 4,⁷⁸ so $-0.25 \leq \beta \leq 0.5$. However, we observe, for example, that $\beta(1.4 \text{ eV}) = -0.55 \pm 0.07$ for the (000) band. Haas and Gericke report broader lines in the (010) spectrum, but do not offer an analysis of the line shapes for this band. There are two additional factors that must be noted here. In the limit of excitation of single rotational levels, the angular distribution will vary markedly with J' .⁷⁹⁻⁸¹ Our current measurements were done at high dissociation laser fluences, where many individual rotational transitions are power broadened into one broad feature, however, so it is not necessary to explicitly consider the J' dependence of the angular distribution. At these higher laser powers, the anisotropy also may be reduced somewhat by saturation,⁸⁰ so the range in β values may actually be larger than indicated in Fig. 11.

We can gain some insight into the various dissociation mechanisms in N₃ from the *ab initio* calculations of the N₃ excited states by Petrongolo,³⁷ and from theoretical and experimental work on the isoelectronic N₂O⁺ ion.^{39,82-84} We first consider the spin-allowed channels. In a linear geometry, the N₃ $\tilde{B}^2\Sigma_u^+$ state correlates adiabatically to the N(²P) + N₂ product channel. This channel is energetically accessible from all levels of the \tilde{B} state, so in order to explain the long lifetime of this state, there must be a significant barrier to this dissociation. Indeed, calculations on the $\tilde{A}^2\Sigma_u^+$ state in N₂O⁺ predict a large barrier for the analogous dissociation channel in the linear configuration.³⁹ The N₃ $\tilde{B}^2\Sigma_u^+$ state does not correlate to N(²D) + N₂ products for linear geometries, but this channel may be reached by a conical intersection between the $\tilde{B}^2\Sigma_u^+$ state and a repulsive $\tilde{A}^2\Delta$ surface, both of which have components of A' symmetry when the molecule is bent. One therefore expects that spin-allowed dissociation is promoted by bending motion of the N₃ molecule, and this is consistent with the large amount of N₂ rotational excitation seen in our experiment.

A useful perspective on the spin-forbidden dissociation channel is provided by the work of Guyon and co-workers,³⁹ who used threshold photoelectron-photoion coincidence spectroscopy to study predissociation from vibrationally excited levels of the N₂O⁺ $\tilde{A}^2\Sigma_u^+$ state. They observe mainly spin-forbidden N(⁴S) + NO⁺ product [the spin-allowed N(²D) + NO⁺ channel lies slightly above the \tilde{A} state origin], and the NO⁺ appears to be highly vibrationally excited. This vibrational excitation may be analogous to our observations for the spin-forbidden N(⁴S) + N₂ channel. Based on *ab initio* calculations on collinear N₂O⁺, they believe that the mechanism for spin-forbidden dissociation involves a relatively slow intersystem crossing with a lower-lying, bound ⁴Π state, followed by a rapid predissociation of the ⁴Π by a ⁴Σ⁻ repulsive state that correlates to N(⁴S) + NO⁺. Spin-forbidden dissociation can presumably occur by a similar mechanism in N₃. The calculation by Petrongolo³⁷ predicts that a bound ⁴Π state lies 0.1 eV below the $\tilde{B}^2\Sigma_u^+$ state in the linear configuration, and this state crosses the repulsive ⁴Σ⁻ state which leads to N(⁴S) + N₂. While it is possible that the observation of positive values of β for the (010) band may reflect contributions from a parallel electronic transition directly to this ⁴Π state, that seems unlikely since the (010) band is unperturbed and gives rise to more spin-allowed as opposed to spin-forbidden products.

Various studies on N₂O⁺ imply that spin-forbidden dissociation from the \tilde{A} state may be facilitated by bending motion. For example, calculations by Hopper⁸² indicate that the energy of the ⁴Π state is considerably lower for bent N₂O⁺ geometries, lowering the energy of the $\tilde{A}^2\Sigma_u^+$ crossing. In an emission spectroscopy experiment, Klapstein and Maier⁸³ observed dramatic decreases in the fluorescence lifetime from bend-excited levels of the N₂O⁺ \tilde{A} state, presumably due to higher predissociation rates. This effect has been modeled in calculations by Beswick and co-workers.⁸⁴ With regard to N₃, in Petrongolo's calculation there is a conical intersection between the ⁴Π and repulsive ⁴Σ⁻ states for the linear molecule. If this intersection lies above the N₃ $\tilde{B}^2\Sigma_u^+$ state, bending motion will facilitate dissociation from this state by providing a lower energy pathway around the conical intersection.

In light of the above considerations, it seems not quite so surprising that N₃ predissociation results in a substantial degree of rotational excitation in the N₂ fragment. The more novel feature in our results is the mode-specific effect in which a substantial increase in the N(²D):N(⁴S) ratio results upon excitation of one quantum in the bending vibration. From the above discussion, one expects bend excitation in the $\tilde{B}^2\Sigma_u^+$ state to increase the predissociation rate to both channels, but our results indicate that one quantum of bend increases the ratio of spin-allowed to spin-forbidden rates by a factor of 6. A key question here is whether the selective enhancement of the spin-allowed channel occurs only when the bending mode of the $\tilde{B}^2\Sigma_u^+$ state is excited, or if the N(²D):N(⁴S) ratio depends only on the total vibrational energy of the predissociating state. Since we only examined dissociation from the (000) and (010) levels of the \tilde{B} state, we cannot resolve this unambiguously.

Both vibrational levels lie well above the two product channels, so it seems doubtful that we are seeing a purely energetic effect. In addition, the qualitative change in the angular distributions of the products seen in the two bands suggests fundamentally distinct dissociation mechanisms as a function of N₃ vibronic state. The bending vibration should be particularly effective in promoting N(²D) production if the bottleneck to this channel occurs at the conical intersection between the $\tilde{B}^2\Sigma_u^+$ and repulsive ²Δ surfaces. We therefore lean towards attributing the enhancement of the spin-allowed channel to specific excitation of the bending mode in N₃. A similar effect on spin-forbidden dissociation was seen by Hepburn and co-workers⁴⁰ in their study of CS₂ photodissociation, and has also been observed in the effects of bending excitation on nonadiabatic processes occurring in the direct dissociation of CH₃I and ICN by Butler and co-workers.^{43,85}

VI. CONCLUSION

The detailed predissociation dynamics of the $\tilde{B}^2\Sigma_u^+$ state of N₃ have been investigated using a new time and position sensitive detector in conjunction with our fast radical beam photofragment spectrometer. The detector was calibrated by studying predissociation from the Schumann–Runge band of O₂ and found to have an energy resolution of better than 40 meV. The N₃ results show that spin-forbidden dissociation occurs, with a branching ratio that is sensitive to initial bending vibrational excitation in the $\tilde{B}^2\Sigma_u^+$ state. Two methods of extracting center-of-mass translational energy and angular distributions are discussed. The results show that the N(²D):N(⁴S) branching ratio changes by a factor of 6 when one quantum of the bending vibration is excited. We also obtain angular and N₂ internal energy distributions for each N + N₂ electronic channel. We find considerable rotational excitation in all channels, and considerably more vibrational excitation in the N(⁴S) + N₂ channel relative to the N(²D) + N₂ channel. The mechanism and dynamics of N₃ dissociation is discussed in light of the existing theoretical studies of N₃ and experiments and theory done on the analogous predissociation of the $\tilde{A}^2\Sigma_u^+$ state of N₂O⁺. The mode-selective decomposition observed in N₃, and in the studies of other systems referenced, shows that the predissociation dynamics of many small polyatomic molecules are very sensitive to the excited state potential energy surfaces, and can often be manipulated by state-selective preparation. Future studies of these effects in free radicals will be of great interest, as the higher density of excited electronic states in these open-shell systems may reveal a diverse variety of useful mode-selective phenomena.

ACKNOWLEDGMENTS

This research is supported by the Director, Office of Energy Research, Office of Basic Energy Sciences, Chemical Sciences Division of the U.S. Department of Energy under Contract No. DE-AC03-76SF00098. Additional support is provided by the National Science Foundation under Grant No. CHE-9108145. We gratefully acknowl-

edge the assistance of Dr. Oswald Siegmund of the University of California Berkeley Space Sciences Laboratory in the design and construction of the C-WSA detector and Joe Stock of UCB-SSL for photoetching the C-WSA anodes. We also acknowledge valuable discussions with Dr. Wim van der Zande of the FOM Institute concerning fast-beam kinetic energy spectroscopy.

- 1 R. N. Zare and D. R. Herschbach, *Proc. IEEE* **51**, 173 (1963).
- 2 For recent general reviews, see M. N. R. Ashfold, I. R. Lambert, D. H. Mordant, G. P. Morley, and C. M. Western, *J. Phys. Chem.* **96**, 2938 (1992); R. Bersohn, in *Molecular Photodissociation Dynamics*, edited by M. N. R. Ashfold and J. E. Baggot (Royal Society of London, London, 1987), pp. 1–30.
- 3 G. E. Busch, J. F. Cornelius, R. T. Mahoney, R. I. Morse, D. W. Schlosser, and K. R. Wilson, *Rev. Sci. Instrum.* **41**, 1066 (1970); G. E. Busch and K. R. Wilson, *J. Chem. Phys.* **56**, 3626 (1972).
- 4 A. M. Wodtke and Y. T. Lee, in *Molecular Photodissociation Dynamics*, edited by M. N. R. Ashfold and J. E. Baggot (Royal Society of Chemistry, London, 1987), p. 31.
- 5 H. J. Krautwald, L. Schnieder, K. H. Welge, and M. N. R. Ashfold, *Faraday Discuss. Chem. Soc.* **82**, 99 (1986); L. Schnieder, W. Meier, K. H. Welge, M. N. R. Ashfold, and C. M. Western, *J. Chem. Phys.* **92**, 7027 (1990).
- 6 J. Segall, Y. Wen, R. Lavi, R. Singer, and C. Wittig, *J. Phys. Chem.* **95**, 8078 (1991).
- 7 P. Andresen and R. Schinke, in *Molecular Photodissociation Dynamics*, edited by M. N. R. Ashfold and J. E. Baggot (Royal Society of Chemistry, London, 1987), pp. 1–113; H. Reisler, M. Noble, and C. Wittig, *ibid.*, pp. 139–176.
- 8 J. P. Simons, *J. Phys. Chem.* **91**, 5378 (1987).
- 9 G. E. Hall and P. L. Houston, *Annu. Rev. Phys. Chem.* **40**, 375 (1989).
- 10 D. W. Chandler and P. L. Houston, *J. Chem. Phys.* **87**, 1445 (1987); M. H. M. Janssen, D. H. Parker, G. O. Sitz, S. Stolte, and D. W. Chandler, *J. Phys. Chem.* **95**, 8007 (1991); T. Suzuki, V. P. Hradil, S. A. Hewitt, P. L. Houston, and B. J. Whitaker, *Chem. Phys. Lett.* **187**, 257 (1991).
- 11 X. Liu and R. D. Coombe, *J. Chem. Phys.* **91**, 7534 (1989).
- 12 J. C. Loison, S. H. Kable, P. L. Houston, and I. Burak, *J. Chem. Phys.* **94**, 1796 (1991).
- 13 C.-W. Hsu, C.-L. Liao, Z.-X. Ma, P. J. H. Tjossem, and C. Y. Ng, *Chem. Phys. Lett.* **199**, 78 (1992).
- 14 E. J. Hints, X. Zhao, W. M. Jackson, W. B. Miller, A. M. Wodtke, and Y. T. Lee, *J. Phys. Chem.* **95**, 2799 (1991); R. E. Continetti, B. A. Balko, and Y. T. Lee, *Chem. Phys. Lett.* **182**, 400 (1991); H. F. Davis and Y. T. Lee, *J. Phys. Chem.* **96**, 5681 (1992); H. F. Davis, B. Kim, H. S. Johnstone, and Y. T. Lee, *ibid.* **97**, 2172 (1993).
- 15 R. E. Continetti, D. R. Cyr, R. B. Metz, and D. M. Neumark, *Chem. Phys. Lett.* **182**, 406 (1991).
- 16 D. R. Cyr, R. E. Continetti, R. B. Metz, D. L. Osborn, and D. M. Neumark, *J. Chem. Phys.* **97**, 4937 (1992).
- 17 D. P. DeBruijn and J. Los, *Rev. Sci. Instrum.* **53**, 1020 (1982).
- 18 W. J. van der Zande, W. Koot, and J. Los, *J. Chem. Phys.* **91**, 4597 (1989); L. D. A. Siebbeles, J. M. Schins, W. J. van der Zande, J. Los, and M. Glass-Maujean, *Phys. Rev. A* **44**, 343 (1991), and references therein.
- 19 S. Kornig, J. H. M. Beijersbergen, W. J. Van der Zande, and J. Los, *Int. J. Mass Spectrom. Ion Proc.* **93**, 49 (1989).
- 20 H. Helm and P. C. Cosby, *J. Chem. Phys.* **86**, 6813 (1987).
- 21 X. Liu, M. A. MacDonald, and R. D. Coombe, *J. Phys. Chem.* **96**, 4907 (1992).
- 22 R. D. Bower and T. T. Yang, *J. Opt. Sci. Am. B* **8**, 1583 (1991).
- 23 R. A. Beaman, T. Nelson, D. S. Richards, and D. W. Setser, *J. Phys. Chem.* **92**, 6090 (1987).
- 24 C. R. Brazier, P. F. Bernath, J. B. Burkholder, and C. J. Howard, *J. Chem. Phys.* **89**, 1762 (1988).
- 25 R. Pahnke, S. H. Ashworth, and J. M. Brown, *Chem. Phys. Lett.* **147**, 179 (1988).
- 26 T. Haas and K.-H. Gericke, *Ber. Bunsenges. Phys. Chem.* **95**, 1289 (1991).
- 27 Note that we refer to $2\Sigma_u^+$ as the \tilde{B} state to be consistent with the literature; see, M. E. Jacox, *J. Phys. Chem. Ref. Data* **19**, 1387 (1990).
- 28 B. A. Thrush, *Proc. R. Soc. London, Ser. A* **235**, 143 (1956).
- 29 A. E. Douglas and W. J. Jones, *Can. J. Phys.* **43**, 2216 (1965).
- 30 M. J. Pellerite, R. L. Jackson, and J. I. Brauman, *J. Phys. Chem.* **85**, 1624 (1981).
- 31 R. L. Jackson, M. J. Pellerite, and J. I. Brauman, *J. Am. Chem. Soc.* **103**, 1802 (1981).
- 32 E. Illenberger, P. B. Comita, J. I. Brauman, H.-P. Fenzlaff, M. Heni, N. Heinrich, W. Koch, and G. Frunking, *Ber. Bunsenges. Phys. Chem.* **89**, 1026 (1985).
- 33 Reference 30 gives $\Delta H_{f,298}^0(\text{N}_3) = 112 \pm 5$ kcal/mol. Following Ref. 34, we calculate $\Delta H_{f,0}^0(\text{N}_3) = \Delta H_{f,298}^0(\text{N}_3) + 0.85$ kcal/mol.
- 34 J. M. L. Martin, J. P. Francois, and R. Gijbels, *J. Chem. Phys.* **93**, 4485 (1990).
- 35 U. Kaldor, *Int. J. Quantum Chem. Quantum Chem. Symp.* **24**, 291 (1990).
- 36 G. Chambaud and P. Rosmus, *J. Chem. Phys.* **96**, 77 (1992).
- 37 C. Petrongolo, *J. Mol. Struct.* **175**, 215 (1988).
- 38 R. Tian and J. Michl, *Faraday Discuss. Chem. Soc.* **86**, 113 (1988); R. Tian, J. C. Facelli, and J. Michl, *J. Phys. Chem.* **92**, 4073 (1988).
- 39 M. Richard-Viard, O. Atabek, O. Dutuit, and P. M. Guyon, *J. Chem. Phys.* **93**, 8881 (1990).
- 40 C. Starrs, M. N. Jago, A. Mank, and J. W. Hepburn, *J. Phys. Chem.* **96**, 6526 (1992).
- 41 L. J. Butler, E. J. Hints, S. F. Shane, and Y. T. Lee, *J. Chem. Phys.* **86**, 2051 (1987).
- 42 I. Bar, Y. Cohen, D. David, T. Avusi-Parpar, S. Rosenwaks, and J. J. Valentini, *J. Chem. Phys.* **95**, 3341 (1991).
- 43 M. D. Person, P. W. Kash, and L. J. Butler, *J. Chem. Phys.* **94**, 2557 (1991); P. W. Kash and L. J. Butler, *ibid.* **96**, 8923 (1992).
- 44 M. A. Johnson, M. L. Alexander, and W. C. Lineberger, *Chem. Phys. Lett.* **112**, 285 (1984).
- 45 R. B. Metz, S. E. Bradforth, and D. M. Neumark, *Adv. Chem. Phys.* **81**, 1 (1992).
- 46 L. A. Posey, M. J. Deluca, and M. A. Johnson, *Chem. Phys. Lett.* **131**, 170 (1986).
- 47 R. E. Continetti, D. R. Cyr, and D. M. Neumark, *Rev. Sci. Instrum.* **63**, 1840 (1992).
- 48 J. M. B. Bakker, *J. Phys. E* **6**, 785 (1973); **7**, 364 (1974).
- 49 R. J. Celotta, R. A. Bennett, J. L. Hall, M. W. Siegel, and J. Levine, *Phys. Rev. A* **6**, 631 (1972).
- 50 P. H. Krupenie, *J. Phys. Chem. Ref. Data* **1**, 423 (1972).
- 51 L. J. Richter and W. Ho, *Rev. Sci. Instrum.* **57**, 1469 (1986).
- 52 J. M. Schins, R. B. Vrijen, W. J. Van der Zande, and J. Los, *Surf. Sci.* **280**, 145 (1993).
- 53 C. Martin, P. Jelinsky, M. Lampton, R. F. Malina, and H. O. Anger, *Rev. Sci. Instrum.* **52**, 1067 (1981).
- 54 J. C. Brenot and M. D. Ferguson, *Adv. Chem. Phys.* **82**, 309 (1992).
- 55 M. Lampton and F. Paresce, *Rev. Sci. Instrum.* **45**, 1098 (1974).
- 56 J. G. Timothy, *Opt. Eng.* **24**, 1066 (1985).
- 57 L. D. Gardner, M. M. Graff, and J. L. Kohl, *Rev. Sci. Instrum.* **57**, 177 (1986).
- 58 O. H. W. Siegmund, M. Lampton, J. Bixler, S. Bowyer, and R. F. Malina, *IEEE Trans. Nucl. Sci.* **NS-33**, 724 (1986); J. V. Vallerga, G. C. Kaplan, O. H. W. Siegmund, M. Lampton, and R. F. Malina, *ibid.* **NS-36**, 881 (1989).
- 59 D. F. Ogletree, G. S. Blackman, R. Q. Hwang, U. Starke, G. A. Somorjai, and J. E. Katz, *Rev. Sci. Instrum.* **63**, 104 (1992).
- 60 O. H. W. Siegmund, K. Coburn, and R. F. Malina, *IEEE Trans. Nucl. Sci.* **NS-32**, 443 (1985).
- 61 K. Yoshino, D. E. Freeman, and W. H. Parkinson, *J. Phys. Chem. Ref. Data* **13**, 207 (1984).
- 62 Y. Matsumi and M. Kawasaki, *J. Chem. Phys.* **93**, 2481 (1990); K. Tonokura, N. Shafer, Y. Matsumi, and M. Kawasaki, *ibid.* **95**, 3394 (1991).
- 63 A. M. Wodtke, L. Huwel, H. Schluter, H. Voges, G. Meijer, and P. Andresen, *J. Chem. Phys.* **89**, 1929 (1988); X. Yang, A. M. Wodtke, and L. Huwel, *ibid.* **94**, 2469 (1991).
- 64 Y.-L. Huang and R. J. Gordon, *J. Chem. Phys.* **94**, 2640 (1991).
- 65 S. S.-L. Chiu, A. S.-C. Cheung, M. Finch, M. J. Jamieson, K. Yoshino, A. Dalgarno, and W. H. Parkinson, *J. Chem. Phys.* **97**, 1787 (1992).
- 66 P. C. Cosby and D. L. Huestis, *J. Chem. Phys.* **97**, 6109 (1992).
- 67 R. Harris, M. Blackledge, and J. Generosa, *J. Mol. Spectrosc.* **30**, 506 (1969).

- ⁶⁸D. M. Creek and R. W. Nicholls, Proc. R. Soc. London, Ser. A **341**, 517 (1975).
- ⁶⁹D. J. Leahy, D. R. Cyr, D. L. Osborn, and D. M. Neumark (unpublished).
- ⁷⁰R. N. Zare, Mol. Photochem. **4**, 1 (1972).
- ⁷¹R. E. Continetti, Ph.D. thesis, University of California, Berkeley, 1989.
- ⁷²B. R. Lewis, L. Berzins, J. H. Carver, and S. T. Gibson, J. Quantum Spectrosc. Radiat. Transfer **36**, 187 (1986).
- ⁷³P. Felder, Chem. Phys. **155**, 435 (1991).
- ⁷⁴K. P. Huber and G. Herzberg, *Molecular Spectra and Molecular Structure IV. Constants of Diatomic Molecules* (Van Nostrand Reinhold, New York, 1979), p. 420.
- ⁷⁵M. A. O'Halloran, H. Joswig, and R. N. Zare, J. Chem. Phys. **87**, 303 (1987).
- ⁷⁶S. H. Kable, J.-C. Loison, D. W. Neyer, P. L. Houston, I. Burak, and R. N. Dixon, J. Phys. Chem. **95**, 8013 (1991).
- ⁷⁷M. F. Jarrold, A. J. Illies, and M. T. Bowers, J. Chem. Phys. **82**, 1832 (1985).
- ⁷⁸S.-C. Yang and R. Bersohn, J. Chem. Phys. **61**, 4400 (1974).
- ⁷⁹M. D. Marshall, E. J. Bohac, and R. E. Miller, J. Chem. Phys. **97**, 3307 (1992).
- ⁸⁰J. H. Ling and K. R. Wilson, J. Chem. Phys. **65**, 881 (1976).
- ⁸¹T. J. Butenhoff, K. L. Carleton, R. D. Van Zee, and C. B. Moore, J. Chem. Phys. **94**, 1947 (1991).
- ⁸²D. G. Hopper, J. Chem. Phys. **76**, 1068 (1982).
- ⁸³D. Klapstein and J. P. Maier, Chem. Phys. Lett. **83**, 590 (1981).
- ⁸⁴J. A. Beswick and M. Horani, Chem. Phys. Lett. **78**, 4 (1981); S. Miret-Artes, G. Delgado-Barrio, O. Atabek, and J. A. Beswick, *ibid.* **98**, 554 (1983).
- ⁸⁵Recent theoretical treatments of these nonadiabatic processes can be found in S. Yabushita, and K. Morokuma, Chem. Phys. Lett. **175**, 518 (1990); H. Guo, J. Chem. Phys. **96**, 6629 (1992).